Ionic coherence in resonant above-threshold attosecond ionization spectroscopy

Saad Mehmood,[1] Eva Lindroth,[2] and Luca Argenti[1,3,*]
[1]*Department of Physics, University of Central Florida, Orlando, Florida 32816, USA*
[2]*Department of Physics, Stockholm University, AlbaNova University Center, SE-10691 Stockholm, Sweden*
[3]*CREOL, University of Central Florida, Orlando, Florida 32816, USA*

(Received 27 September 2022; revised 8 February 2023; accepted 23 February 2023; published 6 March 2023)

The ionization of atoms with sequences of attosecond pulses gives rise to excited ionic states that are entangled with the emitted photoelectron. Still, the ionic ensemble preserves some coherence that can be controlled through the laser parameters. In helium, control of the $2s/2p$ He^+ coherence is mediated by the autoionizing states below the $N = 2$ threshold [Phys. Rev. Res. **3**, 023233 (2021)]. In the present work we study the role of the resonances both below and above the $N = 3$ threshold on the coherence of the $N = 3$ He^+ ion, in the attosecond pump-probe ionization of the helium atom, which we simulate using the NEWSTOCK *ab initio* code. Due to the fine-structure splitting of the $N = 3$ He^+ level, the ionic dipole beats on a picosecond timescale. We show how, from the dipole beating, it is possible to reconstruct the polarization of the ion at its inception.

DOI: 10.1103/PhysRevA.107.033103

I. INTRODUCTION

The typical spectrum of a polyelectronic atom comprises several excited bound and metastable states. In the vicinity of an ionization threshold, many of these states can be coherently populated by short light pulses, giving rise to electronic motion that unfolds on a subfemtosecond timescale [1–3]. The advent of tabletop sources of attosecond light pulses has unlocked the door to the observation and control of such electronic motion at its natural time scale [1,4–10]. Once the production of attosecond pulses became routine, attosecond extreme ultravoilet (XUV) pump infrared (IR) probe photoelectron spectroscopies emerged as a powerful tool to explore attosecond dynamics at the nano [11,12] and the molecular scale [13–17]. The generation of coherent superposition of electronic states above the ionization threshold bears the promise of quantum control in the electronic continuum. However, since ions and photoelectrons normally form entangled pairs, either of the photofragments is only partially coherent, with their coherence depending on the parameters of the ionization process [18,19].

In a recent work, we examined how the autoionizing states below the $N = 2$ threshold of the helium atom could be leveraged to control the relative coherence between the $2s$ and $2p$ states of the He^+ ion [20]. In this work, we explore the entangled character of the wave function for a system comprised of the He^+ parent ion in the $N = 3$ manifold and the photoelectron that emerge from the ionization of a helium atom. We also describe a protocol to reconstruct the density matrix of the He^+ ensemble from the measurement of the picosecond time-scale beatings of its dipole moment, which are caused by the fine splitting of the $N = 3$ level.

On a femtosecond timescale, the effects of spin-orbit interactions do not manifest themselves, and hence the coherence between He^+ ionic states with the same principal quantum number appears as a permanent polarization of the ion. The ion can be produced in such a polarized state by triggering ionization in the presence of a strong infrared dressing pulse with a pulse of extreme ultraviolet radiation with duration shorter than half the period of the IR pulse [21,22]. Alternatively, it is possible to exploit the interference between different resonant ionization paths [20,23,24].

Resonant states play a crucial role in multiphoton ionization since, in contrast to photofragments, they are fully coherent states and they have long lifetimes compared with direct-ionization photoelectron wave packets, which leave the interaction region in a matter of few tens of attoseconds [25–30]. Such long-lived metastable states provide resonant multiphoton pathways for ionization in atoms [31,32], ultrafast decay of electrons [33], and dissociative photoionization in molecules [34,35].

A variety of experiments have studied autoionizing resonances in an attempt to resolve the electron-correlation-driven dynamics that underpins Auger decay [26,30,36–38]. In the present study, we examine the interplay between the autoionizing states below and above the $N = 3$ threshold in multiphoton ionization paths that are resonant both in the intermediate and in the final states. We do so by comparing the relative coherences of the He^+ $3s$, $3p_m$, and $3d_m$ states computed either in the absence or in the presence of the resonances above the N = 3 threshold.

As in the case of the $N = 2$ manifold [20], in the nonrelativistic limit, $N = 3$ He^+ parent-ion states are degenerate, and hence their coherence results in a permanent dipole moment. On a timescale of few picoseconds, the dipole moment fluctuates even in the absence of external fields, due to fine-structure terms, and in particular to spin-orbit interaction [39]. In contrast to the $N = 2$ case, however, the reconstruction

*luca.argenti@ucf.edu

of the He^+ density matrix from the sole observation of the system's dipole fluctuations cannot be complete. Indeed, the coherence between the $3s$ and $3d_m$ states does not result in any dipole emission. Here we describe an algorithm to maximally reconstruct the initial ionic coherences from the optical observations alone.

The paper is organized as follows. Section II offers an overview of the *ab initio* theoretical and numerical methods used to compute, at the end of a pulse sequence, the photoelectron distribution entangled with each ion. Section III describes the pump-probe scheme used for the simulations. Section IV discusses the partial photoelectron distributions as well as the corresponding reduced density matrix for the ion. Section V describes the reconstruction of the ionic coherence from the picosecond beating of the ion dipole. Section VI summarizes the conclusions and perspectives of this work. Finally, the Appendix describes in detail the algorithm used to reconstruct, from the observation of the electric dipole beatings, the off-diagonal elements of the ion density matrix.

II. THEORETICAL METHODS

This section describes the calculation of bound and single-ionization states of the helium atom using the close-coupling approach [25,40,41]. The theory and implementation of a time-dependent close-coupling code dedicated to helium, and of the NEWSTOCK code, for general polyelectronic atoms, is described elsewhere [20,42,43]. Here we offer a brief summary of the protocols implemented in NEWSTOCK , adapted to the helium atom.

A. Structural calculations

The close-coupling (CC) representation of a single ionization function $\Psi(x_1, x_2; t)$ for the helium atom is

$$\Psi(x_1, x_2; t) = \frac{1 - \hat{\mathcal{P}}_{12}}{\sqrt{2}} \sum_{\Gamma\alpha} \Phi^{\Gamma}_{\alpha}(x_1; \hat{r}_2, \zeta_2)\varphi^{\Gamma}_{\alpha}(r_2; t) + \sum_{\Gamma i} \chi^{\Gamma}_i(x_1, x_2)c^{\Gamma}_i(t), \tag{1}$$

where $x_i = (\vec{r}_i, \zeta_i)$ is the spatial-spin component of the i th electron, $\hat{\mathcal{P}}$ swaps the coordinates of the two electrons, $\Phi^{\Gamma}_{\alpha}(x_1; \hat{r}_2, \zeta_2)$ is a channel function in which the orbital and spin angular momentum of the ion are coupled to the photoelectrons,

$$\Phi^{\Gamma}_{\alpha}(x_1; \hat{r}_2, \zeta_2) = R_{N_\alpha L_\alpha}(r_1)\mathcal{Y}^{LM}_{L_\alpha \ell_\alpha}(\hat{r}_1, \hat{r}_2)\Theta_{S\Sigma}(\zeta_1, \zeta_2), \tag{2}$$

and $\varphi^{\Gamma}_{\alpha}(r_2; t)$ is the radial component of the photoelectron wave function in channel (Γ, α) [28,30,44].

In (2), $R_{n\ell}(r)$ is an hydrogenic radial wave function with principal quantum number n, orbital angular momentum ℓ, for a system with nuclear charge $Z = 2$. The functions $\mathcal{Y}^{c\gamma}_{ab}(\hat{r}_1, \hat{r}_2)$ and $\Theta_{S\Sigma}(\zeta_1, \zeta_2)$ are bipolar spherical harmonics and two-electron spin functions [45], respectively,

$$\begin{aligned} \mathcal{Y}^{LM}_{\ell_1\ell_2}(\hat{r}_1, \hat{r}_2) &= \sum_{m_1 m_2} C^{LM}_{\ell_1 m_1, \ell_2 m_2} Y_{\ell_1 m_1}(\hat{r}_1) Y_{\ell_2 m_2}(\hat{r}_2), \\ \Theta_{S\Sigma}(\zeta_1, \zeta_2) &= \sum_{\sigma_1\sigma_2} C^{S\Sigma}_{\frac{1}{2}\sigma_1, \frac{1}{2}\sigma_2} {}^2\chi_{\sigma_1}(\zeta_1)\,{}^2\chi_{\sigma_2}(\zeta_2), \end{aligned} \tag{3}$$

where $Y_{\ell m}(\hat{r})$ are spherical harmonics, ${}^2\chi_\sigma(\zeta) = \langle\zeta|\sigma\rangle = \delta_{\zeta\sigma}$ are spin-$\frac{1}{2}$ functions, and $C^{c\gamma}_{a\alpha,b\beta}$ are Clebsch-Gordan coefficients [45].

The collective symmetry label Γ stands for the quantum numbers of the two-electron system, i.e., the total parity Π and the total orbital and spin angular momenta and projections L, S, Σ, and M, whereas α identifies the parent-ion shell $N_\alpha L_\alpha$ and the photoelectron orbital angular momentum ℓ_α. Finally, the functions $\chi_i(x_1, x_2)$ are symmetry-adapted two-electron configurations state functions (CSF) ${}^{2S+1}(n_1\ell_1, n_2\ell_2)_{LM}$ with principal quantum numbers n_i and angular quantum numbers ℓ_i restricted to $n_i \leqslant N_{\max}$, $\ell_1 \leqslant L_{\max}$.

The CC wave functions (1) and the time evolution of helium from an initial bound state as a result of the interaction with external fields are computed with NEWSTOCK [41,42]. In this work, the time-dependent Hamiltonian $H(t)$ comprises the electrostatic Hamiltonian H_0 and the velocity-gauge interaction Hamiltonian H_I,

$$\begin{aligned} H(t) &= H_0 + H_I(t) \\ H_0 &= \frac{p_1^2 + p_2^2}{2} - \frac{2}{r_1} - \frac{2}{r_2} + \frac{1}{r_{12}} \\ H_I(t) &= \alpha\vec{A}(t) \cdot (\vec{p}_1 + \vec{p}_2), \end{aligned} \tag{4}$$

where $\vec{A}(t)$ is the vector potential and α is the fine-structure constant, $\alpha = e^2/\hbar c \approx 1/137$ [46]. Unless stated otherwise, atomic units and the Gauss system are used. The reduced radial function of all one-electron orbitals, $r\varphi(r)$, is expanded in B-splines [40,47,48].

In this work, two CSF bases are used. A first smaller set, referred to as case 1, comprises all the configurations of the form $n\ell i\ell'$, with $n \leqslant 3$, $\ell \leqslant 2$, $\ell' \leqslant 5$, and the index i runs over all the radial functions in the quantization box (several hundred), which do not necessarily resemble hydrogenic bound orbitals. This first basis is unable to represent any resonance above the $N = 3$ threshold, as these are known to originate from configurations of the form $n\ell n'\ell'$, with $n \geqslant 4$ [49]. A second, larger basis, referred to as case 2, comprises all the configurations of the form $n\ell i\ell'$, with $n \leqslant 4$, $\ell \leqslant 3$, $\ell' \leqslant 5$, and the index i has the same meaning as above. This second basis does give rise to resonances between the $N = 3$ and $N = 4$ thresholds, most of which have dominant configuration $4\ell n'\ell'$.

This energy interval includes also a couple of so-called intruder states of the form $5\ell 5\ell'$ [40,49,50]. These intruder states, however, fall close to the $N = 4$ threshold, which is not reached by our pump-probe scheme, and hence are not expected to play any major role here. Since the He^+ ion has only one electron, within the electrostatic approximation, its eigenstates, numerically computed using the ATSP2K package [51], are virtually exact.

In the present work we will focus our attention on the effects of the probe pulse to the lowest perturbative order. For this reason, for both cases, we will consider only the total symmetries ${}^1S^e$, ${}^1P^o$, and ${}^1D^e$, using ${}^1F^o$ only to check the convergence of our simulations. Notice that we are not including any ${}^1P^e$, ${}^1D^o$, or ${}^1F^e$ state in the basis because non-natural symmetries (i.e., whose parity differs from the total angular momentum parity) cannot be populated by collinearly

polarized light pulses starting from an initial state with magnetic quantum number $M = 0$.

Each symmetric space comprises a localized channel constructed by adding, in all possible ways, an electron to a CSF configuration in any of the $3s$, $3p$, $3d$, $4s$, and $4p$ active orbitals. There are 20 (10), 20 (8), 21 (7), and 12 (2) such states for the $^1S^e$, $^1P^o$, $^1D^e$, and $^1F^o$ symmetries for the case-2 (case-1) basis, respectively. To represent the radial part of both bound and continuum atomic orbitals, we use B-splines of order 7 with asymptotic separation between consecutive nodes of 0.4 a.u., up to a maximum radius of 300 a.u. With this choice, each partial-wave channel comprises approximately 1285 states.

The NEWSTOCK package builds the field-free Hamiltonian matrix $\mathbf{H}^{\Gamma}_{ij} = \langle \Psi^{\Gamma}_i | \hat{H}_0 | \Psi^{\Gamma}_j \rangle$ for each of the four main symmetries $\Gamma = {}^1S^e$, $^1P^o$, $^1D^e$, $^1F^o$, where Ψ^{Γ}_j is any of the functions in the generalized close-coupling space with symmetry Γ, as well as the reduced dipole matrix elements $\langle \Psi^{\Gamma}_i \| P_1 \| \Psi^{\Gamma'}_j \rangle$ between S and P, P and D, and D and F states. For case 1 (no $N = 4$ channels) the electronic configuration basis comprises, beyond the minimal set of close-coupling channels $N\ell\epsilon_{\ell'}$ with $N \leqslant 3$, also the full configuration interaction (CI) set of configuration $n\ell n'\ell'$ constructed from all the localized orbitals with orbital angular momentum $\ell, \ell' \leqslant 5$, and total angular momentum L up to 3. The overall size of the $^1L^{\pi}$ spaces, with $L = 0$, 1, 2 and 3, are 4766, 7147, 7946, and 7948, respectively, for a total size of 27 807. The energy of the ground state is $E_g = -2.8866308$ a.u. For case 2, the basis includes also the $N = 4$ close-coupling channels, which brings the size of the $^1L^{\pi}$ spaces, with $L = 0$, 1, 2 and 3, to 7940, 12 700, 15 090, and 15 093, respectively (total size 50 823). The energy of the ground state changes only marginally, $E_g = -2.887340$ a.u. This value is to be compared on the one side with the Hartree-Fock limit, $E_{g,\mathrm{HF}} = -2.86180$ a.u. [52], and on the other side with the accurate limit for $\ell_{\max} = 3$, which is the maximum orbital angular momentum represented in $^1S^e$ configurations, in our calculations, $E_{g,\ell\leqslant 3} = 2.903321$ a.u. [52]. This means that our ground state energy includes about 62% of the theoretical maximum for $\ell_{\max} = 3$. This discrepancy is to be mostly attributed to the convergence in the radial basis which, for the localized configurations $n\ell n'\ell'$, is restricted to $n, n' \leqslant 3$, for case 1 and $n, n' \leqslant 4$, for case 2.

B. Temporal evolution

The initial ground state is obtained by diagonalizing the Hamiltonian in the $^1S^e$ sector of the full close-coupling space. The time evolution of the atomic wave function, from the initial ground state, under the influence of the external pulses is governed by the time-dependent Schrödinger equation (TDSE),

$$i\partial_t |\Psi(t)\rangle = H(t)|\Psi(t)\rangle, \tag{5}$$

which is integrated numerically in time steps of the duration of approximately $dt = 0.033$ a.u., using a unitary second-order exponential split operator. The propagator includes also the effect of a complex absorption potential (CAP), confined to the last 50 Bohr radii of the spherical quantization box, which prevents unphysical reflections from the box walls,

$$\begin{aligned} |\Psi(t+dt)\rangle &= U_{\mathrm{CAP}}(dt)\, U(t+dt,t)|\Psi(t_0)\rangle \\ U(t+dt,t) &= e^{-i\,H_0\,dt/2} e^{-i\,H_I(t+dt/2)\,dt} e^{-i\,H_0\,dt/2} \\ U_{\mathrm{CAP}}(dt) &= e^{-iV_{\mathrm{CAP}}dt} \\ V_{\mathrm{CAP}} &= -ic \sum_{i=1}^{2} \theta(r_i - R_{\mathrm{CAP}})(r_i - R_{\mathrm{CAP}})^2, \end{aligned} \tag{6}$$

where $\theta(x)$ is the Heaviside step function [$\theta(x) = 0$ if $x < 0$, $\theta(x) = 1$ if $x > 0$], c is a positive real parameter, $c = 5 \times 10^{-4}$, and $R_{\mathrm{CAP}} = 250$ a.u.. The reflection by the CAP itself and by the box boundary are both negligible. The unitary evolution under the action of the dipole operator is evaluated with an iterative Krylov method [25].

C. Partitioning of the time-dependent wave function

The photoelectron component of the wave function grows rapidly in size. Indeed, in 100 fs, the typical size of an attosecond pump-probe time-delay scan, a photoelectron with asymptotic energy of about 1 a.u. ($\simeq 27$ eV) covers a distance of more than 4000 Bohr radii. In order to recover the spectrum of the photoelectron, the whole wave function must be preserved. On the other hand, once the photoelectron has reached a distance of a few hundred atomic units, the coupling between different channels is negligible and hence the electron propagates in what is essentially a pure monopolar electrostatic potential plus the potential due to the external radiation field. In these conditions, an explicit numerical representation of the whole photoelectron wave packet is highly impractical. Luckily, at large distances, we can exploit a useful approximation, which we describe below. The propagator from an initial time t_0 to a final time t reads

$$U(t,t_0) = \hat{T} \exp\left[-i \int_{t_0}^{t} dt_1 H(t_1)\right], \tag{7}$$

where $\hat{T}$ exp is the time-ordered exponential [53]. This propagator can be factorized using Magnus expansion [54],

$$U(t,t_0) = \exp\left[-i\Omega(t,t_0)\right], \tag{8}$$

where

$$\begin{aligned} \Omega(t,t_0) &= \sum_{n=1}^{\infty} \Omega_n(t,t_0), \\ \Omega_1(t,t_0) &= \int_{t_0}^{t} H(t_1) dt_1 \\ \Omega_2(t,t_0) &= \frac{1}{2i} \int_{t_0}^{t} dt_1 \int_{t_0}^{t_1} dt_2 \left[H(t_1), H(t_2)\right] \\ &\cdots \end{aligned} \tag{9}$$

When the photoelectron is sufficiently far from the associated ion, the time evolution of the electron and that of the ion become independent. The Hamiltonian of the photoelectron, in particular, becomes

$$H(t) = \frac{p^2}{2} - \frac{1}{r} + \alpha \vec{A}(t) \cdot \vec{p}. \tag{10}$$

The commutator between the field-free component of the photoelectron Hamiltonian and the interaction term scales as $1/r^2$, and hence, for a photoelectron sufficiently far from the ion, all higher-order terms in the Magnus expansion become negligible,

$$U(t,t_0) \approx \exp\left[-i\int_{t_0}^{t} H(t)dt\right] = \\ = \exp\left[-i\left(\frac{p^2}{2}-\frac{1}{r}\right)(t-t_0) - i\vec{p}\cdot\int_{t_0}^{t}\vec{A}(t)dt\right]. \tag{11}$$

Whenever the integral of the vector potential between an initial and a final time vanishes, therefore, the interaction term itself vanishes, and hence the photoelectron propagator can be accurately approximated by the field-free propagator alone. We take advantage of this circumstance in our simulations because about every half period of the Mid-InfraRed (MIR) field t_i the integral $\int_{t_i}^{\infty} A(t')dt'$ does vanish. At these times, we split the wave function into a mid- to short-range ($r \lesssim 150$ a.u.) and a mid- to long-range component ($r \gtrsim 150$ a.u.),

$$\begin{aligned} |\Psi_{0,\mathrm{SR}}(t_0)\rangle &= |\Psi(t_0)\rangle \\ |\Psi_i(t_i)\rangle &= |\Psi_{i,\mathrm{SR}}(t_i)\rangle + |\Psi_{i,\mathrm{LR}}(t_i)\rangle, \\ |\Psi_{i,\mathrm{LR}}(t_i)\rangle &= P|\Psi_{i-1,\mathrm{SR}}(t_i)\rangle, \\ |\Psi_{i,\mathrm{SR}}(t_i)\rangle &= (1-P)|\Psi_{i-1,\mathrm{LR}}(t_i)\rangle, \end{aligned} \tag{12}$$

where P extracts the long-range distance of the wave function. In coordinate representation, in particular

$$\langle x_1, x_2|P = \sum_{i=1,2}\Phi\left(\frac{r_i - R_{\mathrm{MASK}}}{\sigma_{\mathrm{MASK}}}\right)\langle x_1, x_2|, \tag{13}$$

where $\Phi(x)$ is the normal cumulative distribution function, $\Phi(x) = (2\pi)^{-1/2}\int_{-\infty}^{x} e^{-t^2/2}dt$. By choosing $R_{\mathrm{MASK}} = R_{\mathrm{BOX}}/2$, and $1 \ll \sigma_{\mathrm{MASK}} \ll R_{\mathrm{MASK}}$, we ensure that $\Psi_{\mathrm{LR}}(t_i)$ is nonnegligible only at large distances from the ion, that it does not acquire unphysical incoming components (and hence, that under the subsequent evolution it remains at a large distance from the ion), and that $|\Psi_{\mathrm{SR}}(t_i)\rangle$ is negligible in the last third or so of the quantization box.

As explained above, as far as the wave-function long-range components extracted at the times t_i are concerned, to all practical purposes, the field-free and the interaction Hamiltonians commute, and hence the effect of the interaction Hamiltonian itself vanishes. Each of these long-range components therefore can be propagated analytically to the end of the pulse t by means of the field-free evolution operator,

$$|\Psi_{i,\mathrm{LR}}(t)\rangle = e^{-iH_0(t-t_i)}|\Psi_{i,\mathrm{LR}}(t_i)\rangle. \tag{14}$$

Furthermore, once the external pulses are over, the last residual short-range component $\Psi_{N,\mathrm{SR}}(t_N)$ can also be propagated in the same way,

$$|\Psi_{N,\mathrm{SR}}(t)\rangle = e^{-iH_0(t-t_N)}|\Psi_{N,\mathrm{SR}}(t_N)\rangle. \tag{15}$$

This procedure allows us to carry out simulations for long pulses in comparatively small quantization boxes. These propagations can be carried out exactly, since in our approach we operate in a spectral basis.

D. Asymptotic observables

To determine the probability amplitude in interaction representation $\mathcal{A}_{A;\vec{k}\sigma}$ for the coincidence detection of the parent ion in the (M_A, Σ_A) state A and of the photoelectron with asymptotic momentum $\vec{k}$, and with spin projection σ, we project the full wave packet $|\Psi(t)\rangle$ on a complete set of scattering states,

$$\mathcal{A}_{A;\vec{k}\sigma} = e^{i(E_A+\varepsilon)t}\langle\Psi^{-}_{A;\vec{k}\sigma}|\Psi(t)\rangle, \tag{16}$$

where $|\Psi^{-}_{A;\vec{k}\sigma}\rangle$, normalized as $\langle\Psi^{-}_{A;\vec{k}\sigma}|\Psi^{-}_{B;\vec{k}'\sigma'}\rangle = \delta_{AB}\delta^{(3)}(\vec{k}-\vec{k}')\delta_{\sigma\sigma'}$, is a scattering state in which the parent ion and the photoelectron are not angularly or spin coupled, which fulfills incoming boundary conditions [25,55,56]. We can now use the partitioning of the wave function in a last short-range component and many long-range components,

$$|\Psi(t)\rangle = |\Psi_{N,\mathrm{SR}}(t)\rangle + \sum_{i=1}^{N}|\Psi_{i,\mathrm{LR}}(t)\rangle, \tag{17}$$

to compute the amplitude as

$$\mathcal{A}_{A;\vec{k}\sigma} = e^{i(E_A+k^2/2)t_N}\langle\Psi^{-}_{A;\vec{k}\sigma}|\Psi_{N,\mathrm{SR}}(t_N)\rangle \\ + \sum_{i=1}^{N} e^{i(E_A+k^2/2)t_i}\langle\Psi^{-}_{A;\vec{k}\sigma}|\Psi_{i,\mathrm{LR}}(t_i)\rangle. \tag{18}$$

In the simulation of a pump-probe experiment, the wave function depends parametrically on the pump-probe delay τ, $|\Psi(t;\tau)\rangle$, and so do the ionization amplitudes, $\mathcal{A}_{A;\vec{k}\sigma}(\tau)$. The reduced density matrix for the parent-ion ensemble, $\rho_{AB}(\tau)$, is obtained tracing out the photoelectron states [57],

$$\rho_{AB}(\tau) = \sum_{\sigma}\int d^3k\,\mathcal{A}_{A\vec{k}\sigma}(\tau)\mathcal{A}^{*}_{B\vec{k}\sigma}(\tau). \tag{19}$$

In practice, we never evaluate the three-dimensional integral in Eq. (20). Instead, we directly use the ionization amplitudes $\mathcal{A}^{\Gamma}_{\alpha\varepsilon}(\tau) = \langle\Psi^{\Gamma(-)}_{\alpha\varepsilon}|\Psi(t;\tau)\rangle$ to scattering states with well-defined total symmetry and asymptotic photoelectron angular momentum ℓ_α and energy ε,

$$\rho_{AB}(\tau) = \sum_{\Gamma\Gamma'\alpha\beta}\int d\varepsilon\,\mathcal{A}^{\Gamma}_{\alpha\varepsilon}(\tau)\mathcal{A}^{\Gamma'*}_{\beta\varepsilon}(\tau), \tag{20}$$

where the sum over α and β are restricted to the channels generated by coupling the ionic states A and B to the same orbital angular momentum $\ell = \ell_\alpha = \ell_\beta$.

The coherence between ionic states [57,58] is

$$g_{AB}(\tau) = \frac{|\rho_{AB}(\tau)|}{\sqrt{\rho_{AA}(\tau)\rho_{BB}(\tau)}}. \tag{21}$$

When considering ionic states with the same principal quantum number, within the electrostatic approximation, the density matrix $\rho_{AB}(\tau)$ is independent of time even in the Schrödinger representation. Due to the fine-structure terms in the Hamiltonian, H_{fs}, however, even the block of the density matrix with a same principal quantum number undergoes slow periodic oscillations, on a picosecond timescale, reproduced by the unitary transformation

$$\rho(t;\tau) = e^{-iH_{\mathrm{fs}}t}\rho(\tau)e^{iH_{\mathrm{fs}}t}. \tag{22}$$

By the same token, the ion dipole moment is not stationary either, exhibiting fluctuations at the Bohr fine frequencies of the ion, $\langle \mu_z(t;\tau)\rangle = \mathrm{Tr}[\mu_z \rho(t;\tau)]$. In this work, we make a semiempirical approximation to the fine-splitting Hamiltonian by assuming that the split levels originating from a given principal quantum number n are expressed in terms of the corresponding subspace $\{|n\ell m\sigma\rangle\}$, with $\ell < n$, $|m| \leqslant \ell$, $\sigma = \pm\frac{1}{2}$. With this approximation we can write, for the He^+ ion,

$$H_{\mathrm{fs}} \simeq \sum_{n\ell mm'\sigma\sigma' j\mu} |n\ell m\sigma\rangle \langle n\ell m'\sigma'| C^{j\mu}_{\ell m,\frac{1}{2}\sigma} \left(E^{\pi}_{nj} + \frac{2}{n^2}\right) C^{j\mu}_{\ell m',\frac{1}{2}\sigma'} \tag{23}$$

where E^{π}_{nj} is the energy of the sublevel with principal quantum number n, total angular momentum j, and parity $\pi = (-1)^{\ell}$. The time evolution of the He^+ state in the $N = 3$ manifold is discussed more in detail in the Appendix.

III. SIMULATION SCHEME

Figure 1 illustrates the energy scheme of the system, in relation to the transitions above the $N = 3$ threshold promoted by the XUV pump and IR probe pulses, for the two cases examined in this work, either excluding (case 1) or including (case 2) the $N = 4$ close-coupling channels. The comparison between these two cases allows us to highlight the role of the Feshbach resonances above threshold in influencing the polarization of the $N = 3$ ion. A weak single attosecond XUV pulse excites the neutral helium atom from the ground state to the $^1P^o$ continuum in the energy interval between the first autoionizing states in the series converging to the $N = 3$ threshold up to the $N = 4$ threshold. In case 1, the configuration basis does not give rise to any autoionizing state above $N = 3$, whereas case 2 features several resonances from the series converging to $N = 4$, starting from ∼0.5 eV above the $N = 3$ threshold.

The autoionizing states in helium exhibit a large static correlation, i.e., most of them are given by a combination of multiple configurations with comparable coefficients. For this reason, they cannot normally be identified by any single dominant configuration. Still, approximate quantum numbers alternative to the hydrogenic ones can often be used to meaningfully label them. Several such schemes have been proposed. Beyond the original Fano's classification [59], it is worth mentioning the ${}_N(K,T)^A_n$ scheme [60], the hyperspherical scheme [61], the Stark scheme $[N_1N_2m]^A_n$ [49], and the molecular scheme $(n_\lambda n_\mu)^A$ [62,63]. Here we will use the Stark scheme, whose quantum numbers have an intuitive interpretation: in the doubly excited states (DESs) formed by two electrons with principal quantum numbers n_1 and $n_2 \gg n_1$, the outer electron acts as the source of an adiabatic uniform electric field on the inner electron. Due to the anomalous Stark effect, the $n_1\ell$ states split into terms with higher or lower energy, depending on how the inner electron is polarized towards or away from the satellite electron. The Stark states of the inner electron are classified with the parabolic quantum numbers N_1, N_2, and m [64]. Finally, the DES is uniquely identified by its total symmetry (multiplicity, total orbital angular momentum, and parity), by the principal quantum number n of the satellite electron, and by an additional quantum number $A = \pm$, borrowed from the molecular scheme, which specifies whether the DES wave function at $r_1 = r_2$ has an antinode or a node, respectively.

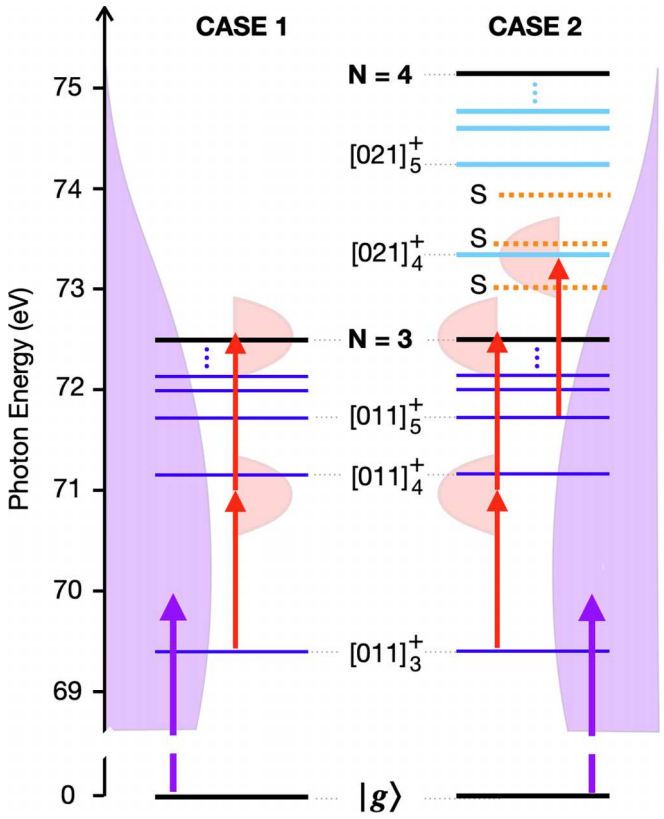

FIG. 1. Energy scheme for the two cases examined in this work. In case 1, only resonances leading up to $N = 3$ ionization threshold are included, whereas case 2 comprises also the resonance series above the $N = 3$ and converging to the $N = 4$ threshold. In either case, an XUV pump pulse, centered just above the $[011]^+_3$ DES, coherently populates several resonances below $N = 3$, as well as directly ionizes the atom to the $N'_L\epsilon'_\ell$ channels. An IR probe pulse subsequently induces transitions from the DES to the $N = 3$ channels, whose interference with the above-threshold amplitudes promoted by the XUV pulse results in the ion polarization. Due to the presence of DES above $N = 3$, case 2 features differ from case 1 in three main respects. First, the one-photon ionization above $N = 3$ is itself altered by the resonances. Second, it supports radiative transitions between DES below and DES above the threshold. Third, it accounts for radiative transitions from the DES above $N = 3$ to the $N = 3$ ionization channels themselves. The effect of these additional interferences depend on the lifetime of and the Bohr frequencies with the $N = 4$ resonances, and hence they can be revealed in the optical response of the ion as a function of the time delay between the pump and the probe pulses.

As discussed in Ref. [20], where ionization in the proximity of the $N = 2$ threshold was considered, a single-photon transition cannot give rise to an asymmetrically polarized ion. Instead, multiphoton transitions are necessary to induce and control any coherence in the $N = 2$ He^+ ion. The case of the ionization above the $N = 3$ threshold, examined here, is different in that the $3s$ and the $3d$ states have the same parity.

Hence, also one-photon transitions can result in the formation of a partly coherent state. Even in this case, however, the parent ion is not electrically polarized.

To polarize the parent ion, it is still necessary to associate the XUV pulse with additional control fields. In our simulation, we include an 800 nm IR probe pulse with a controllable delay with respect to the XUV pulse. The IR pulse promotes nonsequential transition paths to the $N = 3$ ionization channels, when the pump and probe pulses overlap, as well as sequential transition paths that have intermediate DESs in that energy region. Thanks to several interfering multiphoton ionization-excitation paths, a coherence between degenerate opposite-parity ionic states now does emerge.

The XUV pump pulse employed in the simulation has a Gaussian temporal profile, with central frequency $\hbar\omega_{\rm XUV} = 72.0\,{\rm eV}$ (2.646 a.u.), a duration of 970 as [full width at half maximum (FWHM) of the envelope of the intensity, $\text{fwhm}_{\rm XUV}$] with the bandwidth of 1.88 eV, and a peak intensity $I_{\rm XUV} = 0.1\ {\rm TW/cm^2}$. The IR probe pulse has a cosine-squared temporal profile, with central frequency $\hbar\omega_{\rm IR} = 1.55\,{\rm eV}$ (0.057 a.u.), an entire duration of 10.66 fs ($\text{fwhm}_{\rm IR} \approx 3.77$ fs), and peak intensity $I_{\rm IR} = 1\ {\rm GW/cm^2}$.

In this calculation, the photoionization cross section from the ground state to the resonant region below the $N = 3$ threshold is virtually the same for case 1 and case 2, as shown in Fig. 2 in Sec. IV below. We assume, therefore, that despite the missing correlation energy and orbital-relaxation energy in case 1 (we expand the wave function in hydrogenic orbitals for the ion, rather than self-consistent-field orbitals for the neutral), our photoionization results are qualitatively accurate.

IV. RESULTS

In this section, we analyze the effect of above-threshold resonances on the loss of ionic coherence between opposite parity states. We compare the two cases, with and without the inclusion of $(N+1)_L n_\ell$ resonances, with a focus on the ionization channels $N'_L \epsilon'_\ell$ above $N' = 3$. The XUV is broad enough to coherently populate multiple resonances below and above the $N = 3$ ionization threshold. The central energy of the XUV pulse is chosen not to populate any state below the $N = 2$ threshold, where resonances have a large cross section. The one-photon photoionization amplitudes for the two bases are compared in Fig. 2; resonances above $N = 3$ are present in one case (red dashed line) and absent in the other (blue line). The parameters of the resonances below the $N = 3$ case change only slightly between the two cases.

In both cases, the XUV pulse populates the DESs below the $N = 3$ threshold, which the IR probe pulse can probe before their Auger decay. The combined absorption of an XUV photon and the additional exchange of IR photons creates a metastable wave packet that evolves in time with the beating frequencies $\omega_{ij} = E_i - E_j$ between the multiple autoionizing states coherently populated by the pulse sequence. When the atom is ionized, these beatings can be found imprinted in the time delay scan of the photoelectron distribution. In case 2, where we populate resonances above as well as below the $N = 3$ threshold, we observe additional beating frequencies among $N = 4$ resonances as well as between resonances below and above the $N = 3$ threshold.

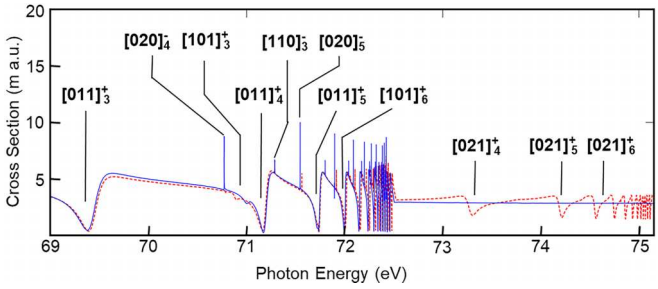

FIG. 2. Comparison of the energy-resolved total photoionization cross section of the helium atom between the $N = 2$ and $N = 4$ threshold, computed with (dashed red line) and without (solid blue line) the $N = 4$ close-coupling channels. $^1P^o$ Doubly excited states, which manifest themselves as Fano profiles in the photoionization cross section, are identified here by their Stark quantum numbers $[N_1 N_2 m]^A_n$.

A combination of attosecond XUV pump and IR probe pulses cause the shake-up ionization of helium through several multiphoton paths, some of which involve intermediate resonances. The interference between direct and multiphoton ionization paths gives rise to new partial coherences between ionic states, compared with those elicited by the XUV pulse alone. The ensemble of He^+ ions emerging from the ionization with principal quantum number $N = 3$, in particular, exhibits coherence between the $3s$ and $3p$ ($m = 0$) states, the $3p$ and $3d$ ($m = 0, 1$) states, and the $3s$ and $3d$ states. Of these coherences, however, only those between states with opposite parity contribute to the expectation value of the ionic dipole. From a measurement of the optical response of the system alone, therefore, it is not possible to reconstruct the density matrix of the ion ensemble to the full. The framed panels in Fig. 3 show the coherence terms $g_{3p_1,3d_1}(\tau, t)$ (a) and (d), $g_{3p_0,3d_0}$ (b) and (e), and $g_{3s,3p_0}(\tau, t)$ (c) and (f), plotted as a function of both the pump-probe delay τ (on a femtosecond timescale) and the real-time t (on a picosecond time scale), computed in case 1 [$N = 4$ channels excluded, Figs. 4(a)–4(c)] and in case 2 [$N = 4$ channels included, Figs. 4(d)–4(f)].

At the low intensity of the IR considered here ($I_{\rm IR} = 10^9 {\rm W/cm^2}$), the dominant cause for the coherence between even and odd states is the overlap of the direct one-photon (XUV) amplitude and the two-photon (XUV + IR) Above-Threshold Ionization (ATI) amplitudes above the $N = 3$ threshold. It is natural, therefore, that all the coherences are modulated, as a function of the pump-probe delay, at twice the frequency of the IR, throughout the time delay scan. When the two pulses overlap, the nonsequential path can contribute to the two-photon transitions, which justifies the stronger amplitude of the modulation. When the two pulses do not overlap, on the other hand, the absorption of an IR photon can only take place from one of the autoionizing states either above or below the threshold, and hence the coherence exhibits weaker modulations. In fact, the quite stronger contrast of the coherence in the sequential regime in case 2 compared to case 1 suggests either that the two-photon amplitude mediated by the $[021]^+_4$ state is stronger than the one mediated by $[011]^+_4$, or that the ATI transitions mediated by the $[011]^+_n$ DESs are much stronger in the presence, in the final states, of the $N = 4$ S

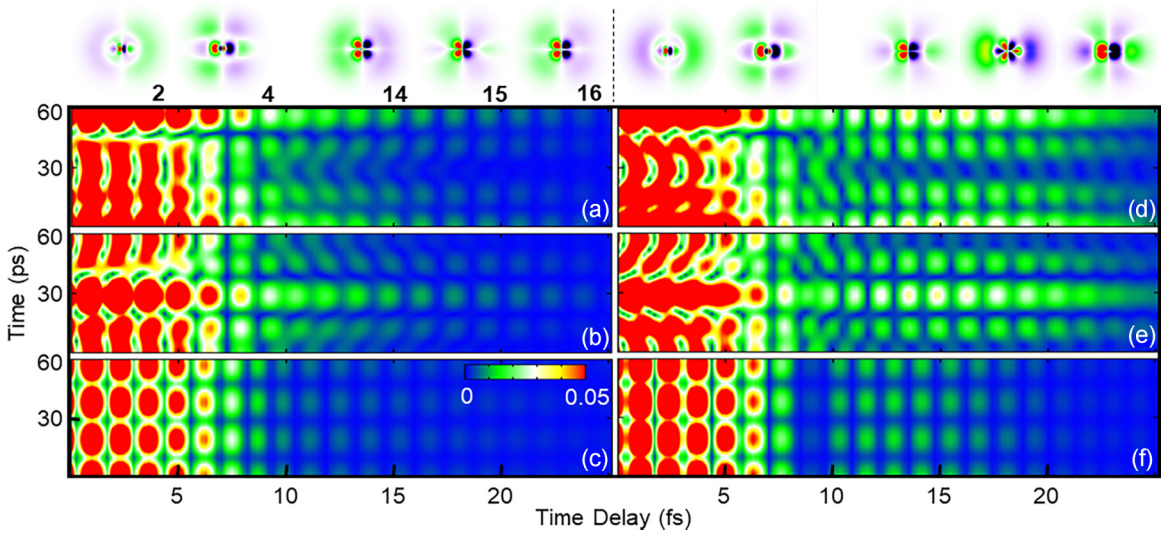

FIG. 3. Partial coherence between states of the He^+ ion with opposite parity and contiguous orbital angular momentum, $g_{3p_1,3d_1}(\tau,t)$ (a) and (d), $g_{3p_0,3d_0}$ (b) and (e), and $g_{3s,3p_0}(\tau,t)$ (c) and (f), which contribute to the ionic dipole. Left panels (a)–(c) correspond to simulations that *exclude* the $4\ell\epsilon'_\ell$ close-coupling channels, and hence that does not account for the contribution from the resonances above the $N=3$ threshold (case 1). Right panels, on the other hand, show the same quantities computed by including the contribution of the $4\ell\epsilon'_\ell$ close-coupling channels, and of the associated above-threshold resonances (case 2). The images on top illustrate the asymmetry of the ionic charge distribution, with respect to the inversion of the laser polarization axis, $\rho(x,y,z)-\rho(x,y,-z)$, at the same selected time delays (2, 4, 14, 15, and 16 fs), in the two cases. The first two snapshots, at 2 and 4 fs, belong to the region where pulses overlap. In this case, the ionic polarization is mostly driven by the dressing field, and it virtually coincides in the two cases. When the probe pulse follows the pump pulse, on the other hand, such as is the case at 14, 15, and 16 fs, the charge asymmetry is visibly different as a result of the significant contribution of the intermediate $4\ell n\ell'$ resonances to the multiphoton transition amplitudes that populate the 3ℓ ionic states. The color scale is linear, with green/yellow/red representing increasingly positive and purple/blue/black increasingly negative excess of charge.

and D resonances [50]. The second most prominent change observed when the $N=4$ channels are included is the appearance of a prominent bump in the coherence for time delays between 10 and 20 fs, and a clear dip in the coherence around $\tau=9$ fs. We attribute this effect to the multiphoton transitions

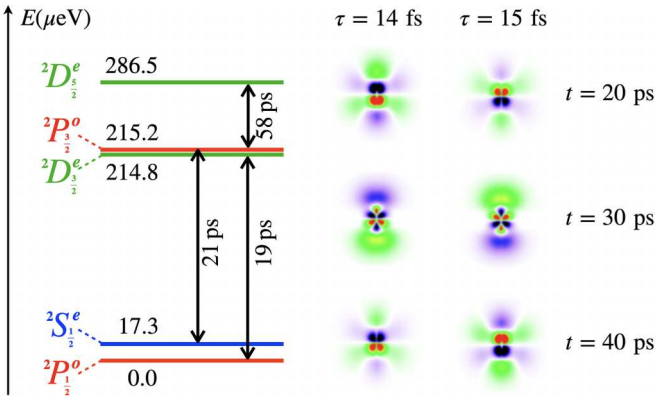

FIG. 4. Left: Energy diagram of the five levels of the He^+ states with principal quantum number $N=3$. The energies, in μeV, are computed from those tabulated in CODATA [46]. Due to this splitting, the charge distribution of the He^+ ions that emerge with $N=3$ from an attosecond photoionization event fluctuates in real time t on a picosecond timescale, as shown on the right for a section of the density in the xy plane at two different values of the pump-probe delay, $\tau=14$ fs and $\tau=15$ fs. The densities are computed by including the $N=4$ channels in the calculations (case 2).

mediated by the $[021]_4^+$ and $[021]_5^+$ $^1P^o$ DESs. Indeed, these states have lifetimes of 6.7 and 11.2 fs, respectively [49], which compare well with the duration of the sequential signal in Figs. 3(d)–3(f). The minimum at 9 fs is arguably due to destructive interference between the polarization effect of the ion induced by the tail of the IR and the resonant multiphoton transition.

The top row in Fig. 3 shows the asymmetry of the ionic charge density $\rho(x,0,z;\tau)-\rho(x,0,-z;\tau)$, immediately after the end of the pulses, as a function of the time delay, where $\rho(x,y,z;\tau)$ is the charge density, and the external fields are polarized along z. In the figure, the x and z axes point up and right, respectively. This quantity illustrates two other aspects of the control of ion coherence. When the two pulses overlap, the inclusion of the $N=4$ resonances does not have any major effect. This circumstance confirms that, up to ~5 fs, the polarizing effect of the IR probe pulse dominates. At higher values of the delay, in absence of the $N=4$ resonances the density asymmetry experiences only minor changes. On the other hand, when the $N=4$ resonances are included, the density asymmetry at the peak of the coherence revival changes drastically, inverting its polarization twice between $\tau=14$, 15, and 16 fs.

As discussed in Sec. II, when the fine structure is taken into account, the $N=3$ states of the He^+ ion are partly resolved in energy, and hence the charge distribution of the subset of the ions with $N=3$ is no longer stationary [see Eq. (22)]. Figure 4 illustrates the relative position of the $N=3$ sublevels, and the characteristic picosecond duration of the

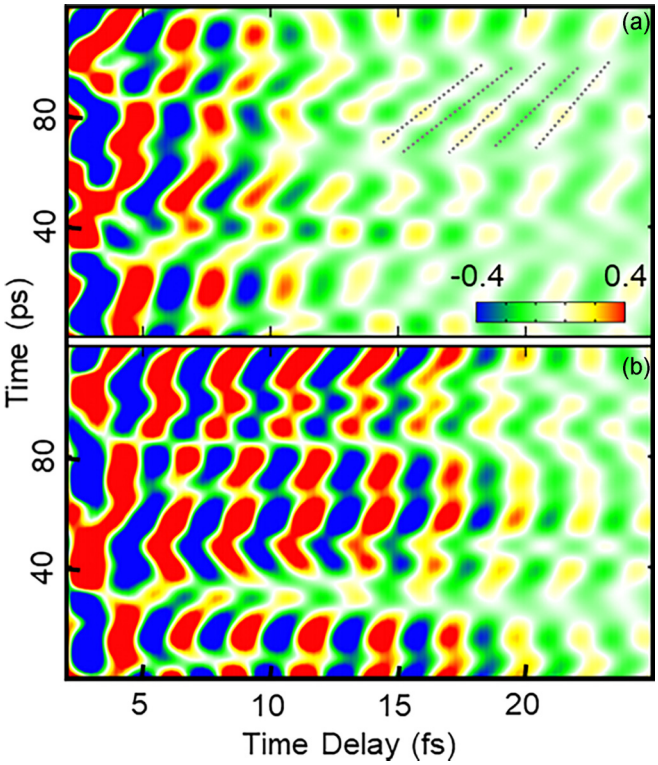

FIG. 5. The expectation value of the electric dipole moment is plotted as a function of time delay and real-time for case 1(top panel) and case 2 (bottom panel). The effect of the IR is more pronounced in case 2, since the $N = 4$ channels enhance the polarization of the $N = 3$ ionic states. The color scale is linear.

beatings they induce. Samples of the charge density computed in case 2, in the case of nonoverlapping pulses, show how the polarization can change substantially as a result of the angular momentum precession. The ${}^2S^e_{\frac{1}{2}} - {}^2P^o_{\frac{3}{2}}$ and ${}^2P^o_{\frac{1}{2}} - {}^2D^e_{\frac{3}{2}}$ splittings are responsible for a periodicity of about 20 ps in the dipole signal, whereas the ${}^2P^o_{\frac{3}{2}} - {}^2D^e_{\frac{5}{2}}$ splitting causes a longer beating, with a period of about 60 ps.

While coherence is not directly measurable, the dipole moment, closely related to coherence between states of opposite parity, is.Figure 5 shows the ionic dipole as a function of pump-probe delay and real time, in both case 1 [Fig. 5(a)] and case 2 [Fig. 5(b)]. As commented above, the dipole fluctuates as a function of real time with two dominant frequency components, with a period of $\simeq 20$ and $\simeq 60$ ps. When the pump and probe pulses overlap, the $\simeq 60$ ps period dominates. A similar phenomenon was observed in the dipole of He^+ in the $N = 2$ level, in pump-probe simulations with a much more intense IR pulse, where a clear checkerboard structure appeared in the dipole spectrum, with independent time and time-delay beatings [20]. Here, this simple checkerboard structure is much less pronounced, due to the comparative weakness of the IR field.

The dipole oscillates also as a function of real time, on a picosecond timescale. When the pulses do not overlap, in case 1 [Fig. 5(a)], when the $N = 4$ channels are not included, we observe an interesting phenomenon: in certain regions of the time/time-delay domain, e.g., $\tau \in [15, 22]$ fs, $t \in [60, 90]$ ps,

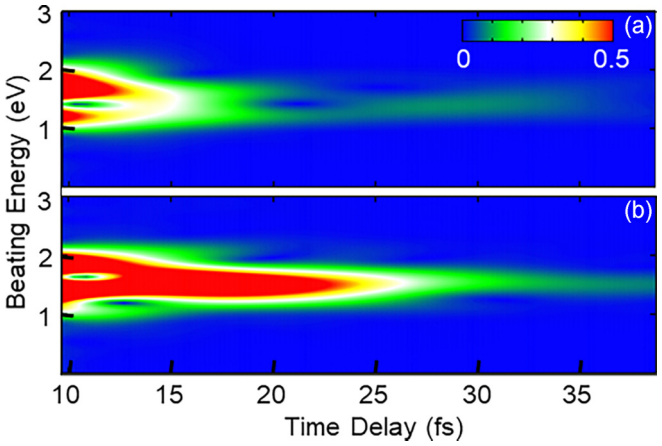

FIG. 6. Window Fourier transform (FWHM = 4.2 fs) of the ion-dipole moment, with respect to the pump-probe time delay, as a function of the window center. (a) $N = 4$ channels excluded. (b) $N = 4$ channels included. The color scale is linear.

the phase of the femtosecond beating maps linearly to that of the picosecond beating, with the period being amplified by a factor of about 6000. Such magnification, if observable, would allow one to determine the polarization of the ionic ensemble at its inception, with subfemtosecond precision, from a microwave spectroscopy measurement conducted with picosecond resolution. As Fig. 5(b) shows, the more realistic case in which the $N = 4$ channels are included is quite less regular. While the phases of the femtosecond and picosecond beating are not independent, the regions in which they exhibit an approximately linear dependence are much smaller.

Figure 6 shows the window Fourier transform of the dipole moment with respect to the time delay,

$$\tilde{\mu}(\tau_w, \omega_\tau) = \frac{1}{\sqrt{8\pi^3}\sigma_w} \int d\tau \, e^{i\omega_\tau \tau - (\tau-\tau_w)^2/2\sigma_w^2} \mu(\tau), \quad (24)$$

where $\sigma_w = 1.8$ fs. The ${}^1P^o$ DESs below the $N = 3$ are common to the two cases, giving rise to beatings with frequencies between 1 and 2 eV. The inclusion of the $N = 4$ channel results in a much stronger signal between 15 and 30 fs, at the central IR energy ($\simeq 1.55$ eV), which supports the interpretation that, at large delays, the dipolar coherence comes predominantly from sequential two-photon transitions (one XUV plus one IR) mediated by the $N = 4$ resonances, and only to a smaller extent by those mediated by the $N = 3$ resonances. In both cases, we observe a loss of both structure and contrast in the coherence at large times. The reason is that when the pump and probe pulses do not overlap, the coherence between $N = 3$ ionic states with opposite parity is entirely due to the indirect multiphoton ionization amplitudes through intermediate DESs. As the delay between the pump and the probe pulse increases, the intermediate DESs decay, thus reducing the contrast, with the population of the shortest-lived resonances decaying faster, hence the reduction in the complexity of the signal. In the case in which the $N = 4$ channels are included, the coherences are stronger and last longer. The reason is that the multiphoton shake-up ionization is amplified by radiative transitions between resonant states below and above the threshold, and by the additional

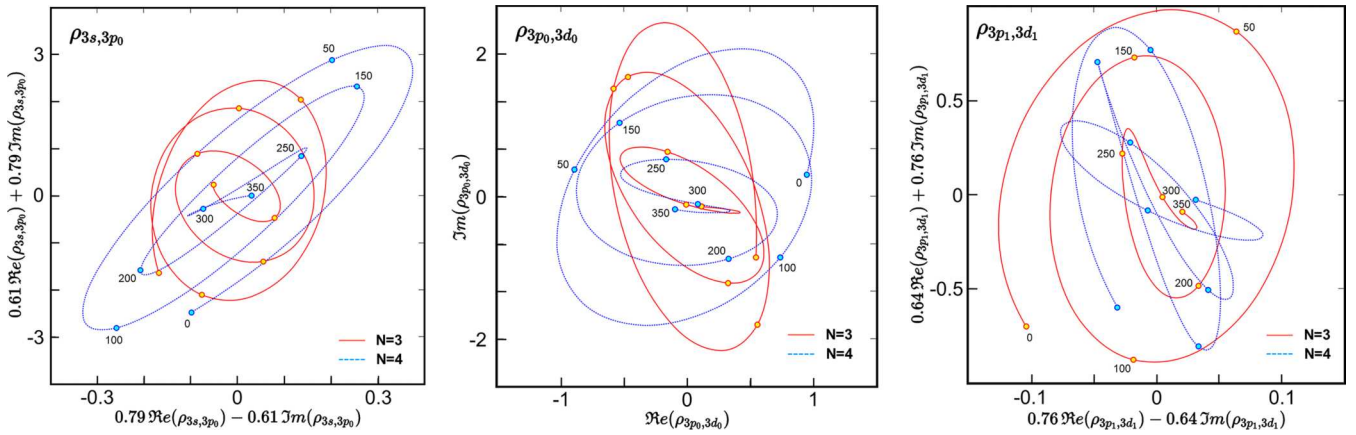

FIG. 7. Polar representation of the trajectory of $e^{i\phi}\,\rho_{3\alpha 3\beta}(\tau)$, as a function of the time delay τ. The two axes are in units of 10^{-3} a.u. In the $(\alpha, \beta) = (3s, 3p_0)$ case, $\phi = 37^\circ$, and for $(\alpha, \beta) = (3p_1, 3d_1)\phi = 40^\circ$, whereas for the $(\alpha, \beta) = (3p_0, 3d_0)$ case, $\phi = 0^\circ$. Notice that the vertical and horizontal axes are on different scales. When the two pulses overlap, ρ_{3s3p_0} has opposite helicity in the $N = 3$ and $N = 4$ cases.

long-lived resonances above $N = 3$. Indeed, when the resonances that lie above the $N = 3$ threshold are included, we observe an additional peak at the energy of 2eV which corresponds to a beating between a resonance from below and above the threshold.

V. RECONSTRUCTION OF IONIC COHERENCE

As described in the previous section, the spin-orbit interaction induces slow fluctuations in the stationary dipole. There are five distinct frequencies ω_{ab} between pairs of states a and b with opposite parity, which appear in the beating of the dipole of the $N = 3$ ionic ensemble. The dipole therefore can be expressed as a real function of these frequencies as follows:

$$\mu(\tau, t) \propto \sum_{ab} z_{ab}(\tau) e^{i\omega_{ab}t}. \tag{25}$$

The time-delay-dependent matrix of coefficients $z_{ab}(\tau)$ is Hermitian, $z_{ab} = z^*_{ba}$. These parameters can be extracted from the beating measured in any sufficiently long finite interval, such as the signal recorded in a time-resolved microwave-spectroscopy measurement of the dipole fluctuation. The Appendix shows in detail how, from the coefficients $z_{ab}(\tau)$, it is possible to maximally reconstruct the density matrix of the ionic ensemble at the time of the ion inception. The result is

$$\boldsymbol{\rho}(\boldsymbol{\alpha}) = \mathbf{U}_R[\mathbf{U}_R^\dagger \mathbf{M} \mathbf{U}_R]^{-1}\mathbf{U}_R^\dagger \mathbf{z} + \mathbf{U}_K \boldsymbol{\alpha}, \tag{26}$$

where $\boldsymbol{\alpha} = (\alpha_1, \alpha_2, \ldots, \alpha_{N_\mathcal{K}})^t$ is a vector of arbitrary complex numbers, with the same dimension as the null space of the dipole expectation value, $\mu = \mathrm{tr}(\boldsymbol{\mu}\boldsymbol{\rho})$, as a functional of the vector space defined by the matrix elements of $\boldsymbol{\rho}$. The eigenvectors over which the particular solution is expressed represent the linear combination of density-matrix elements that can be reconstructed from an all-optical measurement.

The excitation scheme described in Sec. III has a duration of a few tens of femtoseconds, i.e., three orders of magnitude smaller than the period of the spin precession caused by the fine-structure splitting. As long as the electron spin does not affect the excitation process itself, therefore, the dipole expectation value at the end of the pulses is dictated only by the coherence between ionic states with the same spin projection, such as the $3s$, $3p_0$ and $3p_m$, $3d_m$ states, whereas any coherence between states with opposite spin projection, such $3s$ and $3\bar{p}_1$, $3p_m$ and $3\bar{d}_{m+1}$, or $3d_m$ and $3\bar{p}_{m+1}$ states, are supposed to be zero. At larger times, the nonstationary character of the $3p_m$ and $3d_m$ configurations emerges, and the dipole moment is observed to oscillate.

The combinations of density-matrix elements that can be determined using the procedure detailed in the Appendix, for the $N = 3$ He^+ states, are

$$\rho_{3s_0,3p_0}, \qquad \rho_{3s_0,3\bar{p}_1} \tag{27}$$

$$A = \rho_{3p_0,3d_0} - \sqrt{3/2}\,\rho_{3p_0,3\bar{d}_1} \tag{28}$$

$$B = \rho_{3\bar{p}_1,3\bar{d}_1} - \sqrt{2/3}\,\rho_{3\bar{p}_1,3d_0} \tag{29}$$

$$C = \sqrt{3}\rho_{3p_0,3\bar{d}_1} + \rho_{3\bar{p}_1,3d_0}, \tag{30}$$

where, for the suffixes, we use the notation $3\ell_m$ for spin-up states and $3\bar{\ell}_m$ for spin-down states. As said above, our calculations neglect spin-orbit effects during the initial ionization event, and hence all the density-matrix elements between states with opposite spin reconstructed immediately after ionization must vanish. In particular, in our calculation, the C coefficient in (30) should and does vanish. Besides $\rho_{3s_0,3\bar{p}_1}$, therefore, C is a second independent observable measurable with optical methods that is sensitive to fine-structure effects *during* the attosecond-ionization event. Furthermore, even if the fine-structure of the ion did have a role during ionization, it would appreciably affect only the matrix elements that would otherwise vanish, whereas its effect on the other ones would arguably be negligible. For all practical purposes, therefore, the quantities A and B, from Eqs. (28) and (29), coincide with the matrix elements $\rho_{3p_0,3d_0}$ and $\rho_{3\bar{p}_1,3\bar{d}_1} (= \rho_{3p_1,3d_1})$, respectively. The only missing nondiagonal matrix element of ρ that this method cannot reconstruct is $\rho_{3s_0,3d_0}$, since it does not manifest itself in the dipolar response of the ion. To check the consistency of this method, we compared the five reconstructed quantities in Eqs. (27)–(30) with the same exact

quantities computed in our *ab initio* simulations, finding a perfect agreement.

Figure 7 compares the complex value of the nonvanishing off-diagonal density-matrix elements that can be reconstructed with this procedure, $\rho_{3s_0,3p_0}$, $\rho_{3p_0,3d_0}$, and $\rho_{3p_1,3d_1}$, as functions of the pump-probe delay, highlighted by open circles, computed either excluding or including the $N=4$ channels in the calculation. In this representation, it is possible to appreciate a qualitative difference between the two cases when the two pulses overlap: in the case of $N=3$, ρ_{3s3p_0} winds clockwise around the origin, whereas in the case of $N=4$, it goes around the origin counterclockwise. It would be tempting to attribute this result to a hypothetical propensity of the doubly excited states either below or above the $N=3$ threshold to be preferentially photoionized to the $2p$ channel, as it is observed for the $N=2$ case [42]. Indeed, when only resonances below $N=3$ are present, since their photoionization would entail the *absorption* of IR photons, they would contribute to the $3p$ state with an amplitude with argument that increases with the time delay, and in turn so would the phase of $\rho_{3s,3p_0}$. Conversely, when the $N=4$ resonances are present, they would introduce a photoionization amplitude associated to the *emission* of IR photons, with decreasing phase as the time delay increases, resulting in a counterclockwise contribution to $\rho_{3s,3p_0}$. Regardless of whether this interpretation bears any merit for the leftmost panel of Fig. 7, however, it certainly is not sufficient to explain the other two plots. Indeed, while $\rho_{3p_0,3d_0}$ goes around the origin counterclockwise for both case 1 and case 2, $\rho_{3p_1,3d_1}$, which differs from the former only by the m quantum number, exhibits the exact opposite behavior. A definitive interpretation of this phenomenon is beyond the scope of the present work, and will be the subject of future investigations.

VI. CONCLUSION

In this work, we have extended to the $N=3$ excited state our study on the control of the He^+ ion generated in attosecond pump-probe spectroscopy. We have assessed the role of the resonances above the $N=3$ threshold, which converge to the subsequent $N=4$ threshold, and ascertain that they significantly extend the range of time delays beyond which the ionic coherence is enhanced. This phenomenon is understood to be due to the sequential XUV + IR two-photon amplitudes to the $N=3$ channels with even parity, mediated by $N=4$ intermediate autoionizing states. We also describe a generalization of the reconstruction protocol of the density-matrix off-diagonal elements from the picosecond fluctuation of the ionic dipole, which can in principle be measured with microwave spectroscopy. While the reconstruction cannot be complete, owing to the presence of coherences that do not contribute to the expectation value of the dipole, it does allow to reconstruct all the coherences between opposite-parity same-spin states. Furthermore, it is possible to use this reconstruction procedure to measure two independent ratios between opposite-spin and same-spin coherences, namely, $\rho_{3s,3\bar{p}_1}/\rho_{3s,3p_0}$ and $(\sqrt{3}\rho_{3p_0,3\bar{d}_1}+\rho_{3\bar{p}_1,3\bar{d}_0})/\rho_{3p_0,3d_0}$. A nonzero result for these measurements would quantify the role of relativistic effects during the attosecond ionization event itself.

ACKNOWLEDGMENTS

This work is supported by NSF Grant No. 1912507. E.L. acknowledges support from Swedish Research Council Grant No. 2020-03315. Special thanks to UCF ARCC for computing time on the STOKES super computer.

APPENDIX: RECONSTRUCTION MODEL

This Appendix describes the algorithm used to reconstruct the off-diagonal elements of the $N=3$ transition density matrix from the measurement of the asymptotic beating of the ionic electric dipole moment due to the fine-structure splitting of the $N=3$ levels. To illustrate the procedure, let us consider a positive square-integrable window function $W(t)$ that is vanishingly small at any time prior to the end of the pump-probe sequence, such as $W(t)=\phi[(t-t_{W1})/\sigma_W]\phi[(t_{W2}-t)/\sigma_W]$, where $\phi(x)=\frac{1}{\sqrt{2\pi}}\int_{-\infty}^{x}e^{-t^2/2}dt$ is the normal cumulative distribution function. The associated window Fourier transform (WFT) is $\bar{f}(\omega)=\int dt\, f(t)W(t)e^{-i\omega t}$. The WFT of Eq. (25) therefore becomes

$$\bar{\mu}(\tau,\omega)\propto\sum_{i=1}^{5}[c_i(\tau)\widetilde{W}(\Omega_j-\omega)+c_i^*(\tau)\widetilde{W}(\Omega_j+\omega)], \quad \text{(A1)}$$

where $\bar{f}(\omega)=\int dt\, f(t)e^{-i\omega t}$ is the ordinary FT, and the first and second terms correspond to positive and negative frequency, respectively. If the duration of the window step, σ_W, and plateau, $t_{W2}-t_{W1}$, are much larger than the beating period of any two frequencies Ω_i and Ω_j, then Eq. (A1) exhibits an isolated peak for each frequency $\omega=\Omega_j$. Indeed, the FT of the $W(t)$ itself is strongly localized at $\omega=0$. In these conditions,

$$\bar{\mu}(\tau,\Omega_i)\propto c_i(\tau)\widetilde{W}(0), \quad c_i(\tau)=\frac{\bar{\mu}(\tau,\Omega_i)}{\bar{\mu}(\tau,\Omega_j)}c_j(\tau), \quad \text{(A2)}$$

which means that we can reconstruct the amplitude and phase of each oscillation frequency, relative to one of them, used as a reference. In the case of the He^+ $N=2$ states, these conditions can be easily met, since all the fundamental fine-structure frequencies that are visible in the dipole beatings are well separated from each other.

If the aforementioned conditions are not met, such as in the case of the $N=3$ He^+ states, in which at least two pairs of frequencies are very close to each other, a different algorithm is needed. Let us define $\mathbb{M}_{ij}=\widetilde{W}(\Omega_i-\Omega_j)$, $\mathbb{N}_{ij}=\widetilde{W}(\Omega_i+\Omega_j)$, and $\mathbb{b}_i=\bar{\mu}(\tau,\Omega_i)$, with which Eq. (A1) can be cast in matrix form,

$$\mathbb{b}=\mathbb{M}\mathbb{c}+\mathbb{N}\mathbb{c}^\star, \quad \text{(A3)}$$

which can be readily solved by considering separately the real and imaginary part of each vector and matrix, $\mathbb{A}^\Re=\Re e\mathbb{A}$, $\mathbb{A}^\Im=\Im e\mathbb{A}$,

$$\begin{bmatrix}\mathbb{c}^\Re\\ \mathbb{c}^\Im\end{bmatrix}=2\begin{bmatrix}(\mathbb{M}+\mathbb{N})^\Re & (\mathbb{N}-\mathbb{M})^\Im\\ (\mathbb{M}+\mathbb{N})^\Im & (\mathbb{M}-\mathbb{N})^\Re\end{bmatrix}^{-1}\begin{bmatrix}\mathbb{b}^\Re\\ \mathbb{b}^\Im\end{bmatrix}. \quad \text{(A4)}$$

This latter equation gives the correct solution even if the different peaks of $\tilde{\mu}(\tau,\omega)$ overlap.

Once the amplitude $|c_i(\tau)|$ and phase $\arg c_i(\tau)$ are known, we must determine the set of density matrices that are

compatible with these observations. For extremely simple systems, such as He^+ $N = 2$ states, the beating coefficients are enough to reconstruct the phase of the density matrix off-diagonal elements. In a more complex system, such as the one at hand here, the reconstruction cannot be complete because there are more off-diagonal elements than dipole-beating modes.

The slow fluctuations caused by the relativistic interactions can be accurately modeled taking into account that, in the fine-structure basis for the one-electron He^+ system, the energy is diagonal. We call LS the one-electron basis $|L, S, M, \Sigma\rangle$, in which the orbital and intrinsic angular momenta are uncoupled, and fs the basis of the fine-structure states, $|\mathbf{\Phi}\rangle = |\mathbf{LS}\rangle\mathbf{U}$, $H|\mathbf{\Phi}\rangle = |\mathbf{\Phi}\rangle\mathbf{E}$, where $E_{ij} = E_i\delta_{ij}$ is a diagonal matrix with the energy of the fine-structure states on the diagonal, and $\mathbf{U}$ is a unitary matrix whose elements are Clebsh-Gordan coefficients. The density matrix in the LS basis, then, has the simple time dependence

$$\boldsymbol{\rho}^{LS}(\tau, t) = \mathbf{U}e^{-i\mathbf{E}t}\boldsymbol{\rho}^{fs}(\tau, 0)e^{i\mathbf{E}t}\mathbf{U}^\dagger, \tag{A5}$$

where $\boldsymbol{\rho}^{fs}(\tau, 0)$ is the representation of the density matrix in the fine-structure basis. As a consequence, the dipole moment can be written as

$$\mu(\tau, t) = \mathrm{tr}[\mathbf{U}e^{-i\mathbf{E}t}\boldsymbol{\rho}^{fs}(\tau, 0)e^{i\mathbf{E}t}\mathbf{U}^\dagger\boldsymbol{\mu}^{LS}], \tag{A6}$$

or, using the cyclic property of the trace, as

$$\mu(\tau, t) = \mathrm{tr}[\boldsymbol{\rho}^{LS}(\tau, 0)\mathbf{U}e^{i\mathbf{E}t}\mathbf{U}^\dagger\boldsymbol{\mu}^{LS}\mathbf{U}e^{-i\mathbf{E}t}\mathbf{U}^\dagger] \tag{A7}$$

Let us call $\mathbf{P}_a$ the projector on the fine-structure state a in the LS basis, $[\mathbf{P}_a]_{ij} = \mathbf{U}_{ia}\mathbf{U}^*_{ja}$, and let us introduce the matrix $\mathbf{\Omega}^{ab} = \mathbf{P}_a\boldsymbol{\mu}^{LS}\mathbf{P}_b$, where a and b are indices of spin-coupled states. Equation (A7) can be expressed as

$$\mu(\tau, t) = \sum_{ab}\mathrm{tr}[\boldsymbol{\rho}^{LS}(\tau, 0)\,\mathbf{\Omega}^{ab}]\; e^{i\omega_{ab}t}, \tag{A8}$$

where $\omega_{ab} = E_a - E_b$. Following the procedure describe above from Eqs. (25)–(A4), we can extract the complex coefficients z_{ab} of terms in (A8),

$$\mathrm{tr}[\boldsymbol{\rho}^{LS}(\tau, 0)\,\mathbf{\Omega}^{ab}] = z_{ab}(\tau). \tag{A9}$$

We can regard (A9) as a system of linear equations for the unknowns $\boldsymbol{\rho}^{LS}(\tau, 0)$, where $\mathbf{\Omega}^{ab}$ is known analytically and z_{ab} is measured experimentally. Since the dipole moment is sensitive only to coherences between states with opposite parity, it is clear that some of the matrix elements of $\boldsymbol{\rho}$ are not constrained by (A9). In particular, none of the diagonal terms are. To solve (A9) systematically, let us express the density matrix as

$$\boldsymbol{\rho} = \sum_i \mathbb{I}^{ii}\rho_{ii} + \sum_{i<j}\left[(\mathbb{I}^{ij} + \mathbb{I}^{ji})\rho^{\Re}_{ij} + i(\mathbb{I}^{ij} - \mathbb{I}^{ji})\rho^{\Im}_{ij}\right] \tag{A10}$$

where $(\mathbb{I}^{ij})_{kl} = \delta_{ik}\delta_{jl}$, $\rho^{\Re}_{ij} = \Re e(\rho_{ij})$, and $\rho^{\Im}_{ij} = \Im m(\rho_{ij})$, and the indices i and j correspond the LS states, in which spin and orbital angular momenta are not coupled. By replacing (A10) into (A8), we obtain

$$z_{ab} = {\sum_{i<j}}'\mathrm{tr}[(\mathbb{I}^{ij} + \mathbb{I}^{ji})\mathbf{\Omega}^{ab}]\,\rho^{\Re}_{ij} + i{\sum_{i<j}}'\mathrm{tr}[(\mathbb{I}^{ij} - \mathbb{I}^{ji})\mathbf{\Omega}^{ab}]\rho^{\Im}_{ij}, \tag{A11}$$

where we used the fact that $\mathrm{tr}[\mathbb{I}^{ii}\mathbf{\Omega}^{ab}] = 0$, and the prime in the summation indicates that we skip over pairs of states i and j that have the same parity. To avoid redundancy, we can assume that a is an even state and b is odd (only states with opposite parity beat with each other). It is also convenient to order the LS basis such that the even states precede the odd ones. If i and j have even and odd parity, respectively, then the trace $\mathrm{tr}[\mathbb{I}^{ji}\mathbf{\Omega}^{ab}] = 0$. Therefore, we can rewrite (A11) as

$$z_{ab} = \sum_i^e\sum_j^o \mathrm{tr}[\mathbb{I}^{ij}\mathbf{\Omega}^{ab}]\,\rho_{ij}. \tag{A12}$$

The relation has now been cast in the form of a linear system for the complex upper-diagonal components of the density matrix between opposite-parity states. Let us define the superindexes $I = (i, j)$ and $A = (a, b)$, and introduce the notation $M_{AI} = \mathrm{tr}[\mathbb{I}^{ij}\mathbf{\Omega}^{ab}]$ and $\rho_I = \rho_{ij}(\tau, t = 0)$ and $z_A = z_{ab}$. The system (A12) then becomes

$$\mathbf{M}\boldsymbol{\rho} = \mathbf{z} \tag{A13}$$

The matrix $\mathbf{M}$ is rectangular with five rows and six columns. Since $\mathbf{M}$ has more columns than rows, the general solution $\boldsymbol{\rho}$ can only be written up to an arbitrary solution of the associated homogeneous system, $\mathbf{A}\boldsymbol{\rho}_h = 0$,

$$\boldsymbol{\rho} = \boldsymbol{\rho}_p + \boldsymbol{\rho}_h, \tag{A14}$$

where $\boldsymbol{\rho}_p$ is a particular solution. To determine the particular solution and the linear space of homogeneous solutions, we can solve the problem

$$\mathbf{M}^\dagger\mathbf{M}\boldsymbol{\rho} = \mathbf{M}^\dagger\mathbf{z}, \tag{A15}$$

where $\mathbf{S} = \mathbf{M}^\dagger\mathbf{M}$ is a positive definite, symmetric real matrix with a rank smaller than its dimension. $\mathbf{S}$ and $\mathbf{M}$ have the same null space, which is spanned by the $N_\mathcal{K}$ eigenvectors of $\mathbf{S}$, $\mathbf{U}_\mathcal{K}$, with eigenvalue zero. We can search for a particular solution of (A13) in the range of $\mathbf{S}$, $\mathbf{U}_\mathcal{R}$, orthogonal to the null space, $\mathbf{U}^\dagger_\mathcal{R}\mathbf{U}_\mathcal{K} = 0$, which has size $N_\mathcal{R} = N - N_\mathcal{K}$,

$$\boldsymbol{\rho}_p = \mathbf{U}_\mathcal{R}\mathbf{c}. \tag{A16}$$

This expression leads to the following equation for the set of coefficients $\mathbf{c}$:

$$\mathbf{U}^\dagger_R\mathbf{M}\mathbf{U}_R\mathbf{c} = \mathbf{U}^\dagger_R\mathbf{z}, \tag{A17}$$

which is readily solved,

$$\mathbf{c} = [\mathbf{U}^\dagger_R\mathbf{M}\mathbf{U}_R]^{-1}\mathbf{U}^\dagger_R\mathbf{z}. \tag{A18}$$

To summarize, the general solution to (A13) is

$$\boldsymbol{\rho}(\boldsymbol{\alpha}) = \mathbf{U}_R[\mathbf{U}^\dagger_R\mathbf{M}\mathbf{U}_R]^{-1}\mathbf{U}^\dagger_R\mathbf{z} + \mathbf{U}_K\boldsymbol{\alpha}, \tag{A19}$$

where $\boldsymbol{\alpha} = (\alpha_1, \alpha_2, \ldots, \alpha_{N_\mathcal{K}})^t$ is a vector of arbitrary complex numbers, with the same dimension as the null space.

[1] F. Krausz and M. Ivanov, Attosecond physics, Rev. Mod. Phys. **81**, 163 (2009).

[2] R. Pazourek, S. Nagele, and J. Burgdörfer, Attosecond chronoscopy of photoemission, Rev. Mod. Phys. **87**, 765 (2015).

[3] F. Calegari, G. Sansone, S. Stagira, C. Vozzi, and M. Nisoli, Advances in attosecond science, J. Phys. B: At. Mol. Opt. Phys. **49**, 062001 (2016).

[4] F. Lépine, G. Sansone, and M. J. J. Vrakking, Molecular applications of attosecond laser pulses, Chem. Phys. Lett. **578**, 1 (2013).

[5] F. Lépine, M. Y. Ivanov, and M. J. J. Vrakking, Attosecond molecular dynamics: Fact or fiction? Nat. Photonics **8**, 195 (2014).

[6] S. R. Leone, C. W. McCurdy, J. Burgdörfer, L. S. Cederbaum, Z. Chang, N. Dudovich, J. Feist, C. H. Greene, M. Y. Ivanov, R. Kienberger, U. Keller, M. F. Kling, Z.-H. Loh, T. Pfeifer, A. N. Pfeiffer, R. Santra, K. J. Schafer, A. Stolow, U. Thumm, and M. J. J. Vrakking, What will it take to observe processes in "real time"? Nat. Photonics **8**, 162 (2014).

[7] S. R. Leone and D. M. Neumark, Attosecond science in atomic, molecular, and condensed matter physics, Faraday Discuss. **194**, 15 (2016).

[8] M. Nisoli, P. Decleva, F. Calegari, A. Palacios, and F. Martín, Attosecond electron dynamics in molecules, Chem. Rev. **117**, 10760 (2017).

[9] G. Sansone, T. Pfeifer, K. Simeonidis, and A. I. Kuleff, Electron correlation in real time, Chem. Phys. Chem. **13**, 661 (2012).

[10] S. R. Leone and D. M. Neumark, Probing matter with nonlinear spectroscopy, Science **379**, 536 (2023).

[11] M. F. Ciappina, J. A. Pérez-Hernández, A. S. Landsman, W. A. Okell, S. Zherebtsov, B. Förg, J. Schötz, L. Seiffert, T. Fennel, T. Shaaran, T. Zimmermann, A. Chacón, R. Guichard, A. Zaïr, J. W. G. Tisch, J. P. Marangos, T. Witting, A. Braun, S. A. Maier, L. Roso *et al.*, Attosecond physics at the nanoscale, Rep. Prog. Phys. **80**, 054401 (2017).

[12] P. Dombi, Z. Pápa, J. Vogelsang, S. V. Yalunin, M. Sivis, G. Herink, S. Schäfer, P. Groß, C. Ropers, and C. Lienau, Strong-field nano-optics, Rev. Mod. Phys. **92**, 025003 (2020).

[13] S. Haessler, J. Caillat, W. Boutu, C. Giovanetti-Teixeira, T. Ruchon, T. Auguste, Z. Diveki, P. Breger, A. Maquet, B. Carré, R. Taïeb, and P. Salières, Attosecond imaging of molecular electronic wavepackets, Nat. Phys. **6**, 200 (2010).

[14] E. Goulielmakis, M. Schultze, M. Hofstetter, V. S. Yakovlev, J. Gagnon, M. Uiberacker, A. L. Aquila, E. M. Gullikson, D. T. Attwood, R. Kienberger, F. Krausz, and U. Kleineberg, Single-cycle nonlinear optics, Science **320**, 1614 (2008).

[15] J. Itatani, F. Quéré, G. L. Yudin, M. Y. Ivanov, F. Krausz, and P. B. Corkum, Attosecond Streak Camera, Phys. Rev. Lett. **88**, 173903 (2002).

[16] G. Sansone, E. Benedetti, F. Calegari, C. Vozzi, L. Avaldi, R. Flammini, L. Poletto, P. Villoresi, C. Altucci, R. Velotta, S. Stagira, S. De Silvestri, and M. Nisoli, Isolated single-cycle attosecond pulses, Science **314**, 443 (2006).

[17] A. L. Cavalieri, N. Müller, T. Uphues, V. S. Yakovlev, A. Baltuška, B. Horvath, B. Schmidt, L. Blümel, R. Holzwarth, S. Hendel, M. Drescher, U. Kleineberg, P. M. Echenique, R. Kienberger, F. Krausz, and U. Heinzmann, Attosecond spectroscopy in condensed matter, Nature (London) **449**, 1029 (2007).

[18] S. Pabst, M. Lein, and H. J. Wörner, Preparing attosecond coherences by strong-field ionization, Phys. Rev. A **93**, 023412 (2016).

[19] C. Bourassin-Bouchet, L. Barreau, V. Gruson, J.-F. Hergott, F. Quéré, P. Salières, and T. Ruchon, Quantifying Decoherence in Attosecond Metrology, Phys. Rev. X **10**, 031048 (2020).

[20] S. Mehmood, E. Lindroth, and L. Argenti, Coherence control in helium-ion ensembles, Phys. Rev. Res. **3**, 023233 (2021).

[21] M. Ossiander, F. Siegrist, V. Shirvanyan, R. Pazourek, A. Sommer, T. Latka, A. Guggenmos, S. Nagele, J. Feist, J. Burgdörfer, R. Kienberger, and M. Schultze, Attosecond correlation dynamics, Nat. Phys. **13**, 280 (2017).

[22] E. Goulielmakis, Z.-H. Loh, A. Wirth, R. Santra, N. Rohringer, V. S. Yakovlev, S. Zherebtsov, T. Pfeifer, A. M. Azzeer, M. F. Kling, S. R. Leone, and F. Krausz, Real-time observation of valence electron motion, Nature (London) **466**, 739 (2010).

[23] R. Guillemin, P. Decleva, M. Stener, C. Bomme, T. Marin, L. Journel, T. Marchenko, R. K. Kushawaha, K. Jänkälä, N. Trcera, K. P. Bowen, D. W. Lindle, M. N. Piancastelli, and M. Simon, Selecting core-hole localization or delocalization in CS_2 by photofragmentation dynamics, Nat. Commun. **6**, 6166 (2015).

[24] M. Shapiro, Generating and controlling chains of entangled atoms by coherent control techniques, Phys. Rev. A **84**, 053432 (2011).

[25] L. Argenti and E. Lindroth, Ionization Branching Ratio Control with a Resonance Attosecond Clock, Phys. Rev. Lett. **105**, 053002 (2010).

[26] V. Gruson, L. Barreau, Á. Jiménez-Galan, F. Risoud, J. Caillat, A. Maquet, B. Carré, F. Lepetit, J.-F. Hergott, T. Ruchon, L. Argenti, R. Taïeb, F. Martín, and P. Salières, Attosecond dynamics through a Fano resonance: Monitoring the birth of a photoelectron, Science **354**, 734 (2016).

[27] E. Lindroth and L. Argenti, Atomic resonance states and their role in charge-changing processes, in *Advances in Quantum Chemistry*, edited by C. A. Nicolaides, E. Brändas, and J. R. Sabin (Academic Press, New York, 2012), Vol. 63, Chap. 5, pp. 247–308.

[28] A. Jiménez-Galán, L. Argenti, and F. Martín, Modulation of Attosecond Beating in Resonant Two-Photon Ionization, Phys. Rev. Lett. **113**, 263001 (2014).

[29] M. Kotur, D. Guénot, Á. Jiménez-Galán, D. Kroon, E. W. Larsen, M. Louisy, S. Bengtsson, M. Miranda, J. Mauritsson, C. L. Arnold, S. E. Canton, M. Gisselbrecht, T. Carette, J. M. Dahlström, E. Lindroth, A. Maquet, L. Argenti, F. Martín, and A. L'Huillier, Spectral phase measurement of a Fano resonance using tunable attosecond pulses, Nat. Commun. **7**, 10566 (2016).

[30] C. Ott, A. Kaldun, L. Argenti, P. Raith, K. Meyer, M. Laux, Y. Zhang, A. Blättermann, S. Hagstotz, T. Ding, R. Heck, J. Madroñero, F. Martín, and T. Pfeifer, Reconstruction and control of a time-dependent two-electron wave packet, Nature (London) **516**, 374 (2014).

[31] M. Nagasono, E. Suljoti, A. Pietzsch, F. Hennies, M. Wellhöfer, J.-T. Hoeft, M. Martins, W. Wurth, R. Treusch, J. Feldhaus, J. R. Schneider, and A. Föhlisch, Resonant two-photon absorption of extreme-ultraviolet free-electron-laser radiation in helium, Phys. Rev. A **75**, 051406(R) (2007).

[32] K. Hütten, M. Mittermair, S. O. Stock, R. Beerwerth, V. Shirvanyan, J. Riemensberger, A. Duensing, R. Heider, M. S. Wagner, A. Guggenmos, S. Fritzsche, N. M. Kabachnik, R. Kienberger, and B. Bernhardt, Ultrafast quantum control of ionization dynamics in krypton, Nat. Commun. **9**, 719 (2018).

[33] A. Föhlisch, P. Feulner, F. Hennies, A. Fink, D. Menzel, D. Sanchez-Portal, P. M. Echenique, and W. Wurth, Direct observation of electron dynamics in the attosecond domain, Nature (London) **436**, 373 (2005).

[34] G. Sansone, F. Kelkensberg, J. F. Pérez-Torres, F. Morales, M. F. Kling, W. Siu, O. Ghafur, P. Johnsson, M. Swoboda, E. Benedetti, F. Ferrari, F. Lépine, J. L. Sanz-Vicario, S. Zherebtsov, I. Znakovskaya, A. L'Huillier, M. Y. Ivanov, M. Nisoli, F. Martín, and M. J. J. Vrakking, Electron localization following attosecond molecular photoionization, Nature (London) **465**, 763 (2010).

[35] F. Martin, J. Fernandez, T. Havermeier, L. Foucar, T. Weber, K. Kreidi, M. Schoffler, L. Schmidt, T. Jahnke, O. Jagutzki, A. Czasch, E. P. Benis, T. Osipov, A. L. Landers, A. Belkacem, M. H. Prior, H. Schmidt-Bocking, C. L. Cocke, and R. Dorner, Single photon-induced symmetry breaking of H_2 dissociation, Science **315**, 629 (2007).

[36] B. Doughty, L. H. Haber, C. Hackett, and S. R. Leone, Photoelectron angular distributions from autoionizing $4s^1 4p^6 6p^1$ states in atomic krypton probed with femtosecond time resolution, J. Chem. Phys. **134**, 094307 (2011).

[37] M. Wickenhauser, J. Burgdörfer, F. Krausz, and M. Drescher, Attosecond streaking of overlapping Fano resonances, J. Mod. Opt. **53**, 247 (2006).

[38] C. Cirelli, C. Marante, S. Heuser, C. L. M. Petersson, Á. Jiménez-Galán, L. Argenti, S. Zhong, D. Busto, M. Isinger, S. Nandi, S. Maclot, L. Rading, P. Johnsson, M. Gisselbrecht, M. Lucchini, L. Gallmann, J. M. Dahlström, E. Lindroth, A. L'Huillier, F. Martín *et al.*, Anisotropic photoemission time delays close to a Fano resonance, Nat. Commun. **9**, 955 (2018).

[39] G. Drake, *Springer Handbook of Atomic, Molecular, and Optical Physics* (Springer, New York, 2006).

[40] L. Argenti and R. Moccia, K-matrix method with B-splines: σ_N, β_N and resonances in He photoionization below $N = 4$ threshold, J. Phys. B: At. Mol. Opt. Phys. **39**, 2773 (2006).

[41] T. Carette, J. M. Dahlström, L. Argenti, and E. Lindroth, Multiconfigurational Hartree-Fock close-coupling ansatz: Application to the argon photoionization cross section and delays, Phys. Rev. A **87**, 023420 (2013).

[42] L. Argenti and E. Lindroth, arXiv:2105.10847 (2021).

[43] N. Harkema, C. Cariker, E. Lindroth, L. Argenti, and A. Sandhu, Autoionizing Polaritons in Attosecond Atomic Ionization, Phys. Rev. Lett. **127**, 023202 (2021).

[44] L. Argenti, A. Jiménez-Galán, C. Marante, C. Ott, T. Pfeifer, and F. Martín, Dressing effects in the attosecond transient absorption spectra of doubly excited states in helium, Phys. Rev. A **91**, 061403(R) (2015).

[45] D. Varshalovich, A. N. Moskalev, and V. K. Khersonskii, *Quantum theory of angular momentum* (World Scientific, Singapore, 1989), p. 514.

[46] P. J. Mohr, D. B. Newell, and B. N. Taylor, Codata recommended values of the fundamental physical constants: 2014, Rev. Mod. Phys. **88**, 035009 (2016).

[47] C. de Boor, *A Practical Guide to Splines* (Springer, New York, 1978).

[48] H. Bachau, E. Cormier, P. Decleva, J. E. Hansen, and F. Martín, Applications of B-splines in atomic and molecular physics, Rep. Prog. Phys. **64**, 1815 (2001).

[49] J.-M. Rost, K. Schulz, M. Domke, and G. Kaindl, Resonance parameters of photo doubly excited helium, J. Phys. B: At. Mol. Opt. Phys. **30**, 4663 (1997).

[50] A. Bürgers, D. Wintgen, J. M. Rost, A. Burgers, and J. M. Rest, Highly doubly excited S states of the helium atom, J. Phys. B: At. Mol. Opt. Phys. **28**, 3163 (1995).

[51] P. Jönsson, X. He, C. Froese Fischer, and I. P. Grant, The grasp2K relativistic atomic structure package, Comput. Phys. Commun. **177**, 597 (2007).

[52] D. P. Carroll and R. M. Metzger, Piecewise polynomial configuration interaction natural orbital study of $1s^2$ helium, J. Chem. Phys. **71**, 4142 (1979).

[53] J. Sakurai and J. Napolitano, *Modern Quantum Mechanics* (Cambridge University Press, Cambridge, 2017).

[54] S. Blanes, F. Casas, J. Oteo, and J. Ros, The magnus expansion and some of its applications, Phys. Rep. **470**, 151 (2009).

[55] L. Argenti, R. Pazourek, J. Feist, S. Nagele, M. Liertzer, E. Persson, J. Burgdörfer, and E. Lindroth, Photoionization of helium by attosecond pulses: Extraction of spectra from correlated wave functions, Phys. Rev. A **87**, 053405 (2013).

[56] L. Argenti and R. Moccia, He photoionization: β_N and σ_N below $N = 5$ and 6 thresholds, Theor. Chem. Acc. **118**, 485 (2007).

[57] U. Fano, Description of states in quantum mechanics by density matrix and operator techniques, Rev. Mod. Phys. **29**, 74 (1957).

[58] S. Pabst, L. Greenman, P. J. Ho, D. A. Mazziotti, and R. Santra, Decoherence in Attosecond Photoionization, Phys. Rev. Lett. **106**, 053003 (2011).

[59] J. W. Cooper, U. Fano, and F. Prats, Classification of Two-Electron Excitation Levels of Helium, Phys. Rev. Lett. **10**, 518 (1963).

[60] D. R. Herrick, Resonance-channel quantum numbers in electron-hydrogen and proton-hydrogen scattering from group theory of the long-range dipole interaction, Phys. Rev. A **12**, 413 (1975).

[61] C. D. Lin, Correlations of excited electrons. The study of channels in hyperspherical coordinates, Phys. Rev. A **10**, 1986 (1974).

[62] S. Watanabe and C. D. Lin, Demonstration of moleculelike modes of doubly excited states in hyperspherical coordinates, Phys. Rev. A **34**, 823 (1986).

[63] J. M. Rost and J. S. Briggs, Diabatic molecular description of symmetric doubly excited atomic states, J. Phys. B: At. Mol. Opt. Phys. **21**, L233 (1988).

[64] H. A. Bethe and E. E. Salpeter, Atoms in external fields, in *Quantum Mechanics of One- and Two-Electron Atoms* (Springer-Verlag, Berlin, 1957), pp. 205–248.